Available online at www.sciencedirect.com

ScienceDirect

Ceramics International 40 (2014) 3295–3304

CERAMICS INTERNATIONAL

www.elsevier.com/locate/ceramint

Eggshell-membrane-templated synthesis of hierarchically-ordered NiO–$Ce_{0.8}Gd_{0.2}O_{1.9}$ composite powders and their electrochemical performances as SOFC anodes

Manasa K. Rath[a], Byung-Hyun Choi[b], Mi-Jung Ji[b], Ki-Tae Lee[a,c,*]

[a]Division of Advanced Materials Engineering, Chonbuk National University, Jeonbuk 561-756, Korea
[b]Energy Materials Center, Korea Institute of Ceramic Engineering and Technology, Seoul 153-801, Korea
[c]Hydrogen and Fuel Cell Research Center, Chonbuk National University, Jeonbuk 561-756, Korea

Received 2 September 2013; accepted 24 September 2013
Available online 1 October 2013

Abstract

Hierarchically-ordered NiO-$Ce_{0.8}Gd_{0.2}O_{1.9}$ (GDC) composite anode powders were synthesized using eggshell membranes as biotemplates. The morphology of the as-synthesized powders depended on the kind of Ni precursor and the use of EDTA as a chelating agent. Hierarchically-ordered anode powders were obtained from Ni chloride and Ni acetate precursors with EDTA. The Ni–GDC anode synthesized from Ni chloride precursor with EDTA exhibited the lowest polarization resistance at 800 °C and an activation energy of 0.01 Ω cm^2 and 0.74 eV, respectively, in humidified H_2. In accordance with the polarization resistance results, the 0.5-mm thick GDC electrolyte-supported single cell with the Ni–GDC anode synthesized from Ni chloride precursor with EDTA showed a maximum power density of 0.34 W cm^{-2} at 800 °C with humidified H_2 fuel.

Keywords: Solid oxide fuel cells; Anode; Eggshell membrane template; Electrochemical performance

1. Introduction

Solid oxide fuel cells (SOFCs) are energy conversion devices for the conversion of various forms of chemical energy (hydrogen, hydrocarbon, natural gas, bio gas, and city gas) into electrical energy with high efficiency [1,2]. SOFCs have gained attention as a green energy technology due to their high conversion efficiency with no pollutants. A typical SOFC consists of two porous electrodes separated by a dense oxide-ion conducting electrolyte. Oxidation of hydrogen and reduction of oxygen occurs at the anode and cathode, respectively, along with the release of electrons to the external circuit. The state-of-the-art electrolyte, cathode, and anode materials for SOFCs are yttria-stabilized zirconia (YSZ), Sr-doped lanthanum manganite (LSM), and Ni–YSZ cermet, respectively.

A main issue of SOFCs is the lowering of the operation temperature, which is required to improve the reliability, portability, and operational life, and the reduction of the cost of components such as the interconnect, manifold, and sealing materials [3,4]. However, the polarization resistance also increases significantly at low temperatures due to the slow electrode kinetics and high ohmic resistance [5,6]. Since the electrode reaction occurs at a limited site, that is, where the electrode, electrolyte, and gas meet, called the triple phase boundary (TPB), the electrochemical performance strongly depends on the TPB length. Theoretically, the polarization resistance is inversely proportional to the square root of the TPB length, which is based on the Thiele modulus [7,8]. Therefore, it is critical to increase the TPB length to improve anode performance during low-temperature operation.

Considering the concentration polarization and the TPB length, optimization of the anode microstructure is an effective approach for enhancing the overall cell performance [4,9,10].

---

*Corresponding author at: Division of Advanced Materials Engineering, Chonbuk National University, Jeonbuk 561-756, Korea.
Tel.: +82 63 270 2290; fax: +82 63 270 2386.
E-mail address: ktlee71@jbnu.ac.kr (K.-T. Lee).

0272-8842/$ - see front matter © 2013 Elsevier Ltd and Techna Group S.r.l. All rights reserved.
http://dx.doi.org/10.1016/j.ceramint.2013.09.105

Recently, the anode microstructure has been optimized using various techniques, such as the insertion of an anode functional layer with nanostructured composites, the control of porosity and pore size distribution with pore formers, the application of a core–shell morphology [11–19]. Nevertheless, key issues remain, including tailoring of the initial morphology of the anode powder, as it strongly affects the final microstructure of the sintered anode.

With respect to tailoring the morphology, the biotemplate process is a promising technique due to its simplicity and cost effectiveness. There are various types of biotemplates such as wood, leaves, fungi, insects, algae, yeast, bacteria, compound eyes, butterfly wings, and eggshell membranes (ESMs) [20]. ESMs are very unique because of their porous morphology with high specific surface area, environmental benignancy, and inexpensiveness. Generally, ESMs are used to remove hazardous waste from water [21]. ESMs are currently used as templates for inorganic synthesis due to their special features such as water-insolubility, high stability, and very high specific surface area with metal ion sorption capacity [22–27]. In this regard, the ESM template could be adopted to prepare SOFC electrode materials with a tailored morphology. Therefore, the main motivation of this study is to implement the bio-waste ESM as a template, because the initial macro-porous skeleton of ESMs allows the precursor materials to form a replica of the morphology with hierarchical structure and enhances the catalytic activity of SOFC anode. Based on a literature survey, some single-component materials such as $Sm_{0.5}Sr_{0.5}CoO_3$, ZrO_2, and $Ce_xZr_{1-x}O_2$ have been synthesized by the ESM template method [28–30]. However, there have been no reports on the synthesis of NiO–$Ce_{0.8}Gd_{0.2}O_{1.9}$ (GDC) composites using the ESM template method. This study presents the synthesis of hierarchically-ordered NiO–GDC powder by the ESM template method with various initial precursors. The effect of the initial precursors and a chelating agent on the morphology of NiO–GDC was investigated. Additionally, the correlation of electrochemical performance with microstructure is discussed.

2. Experimental procedures

NiO–GDC composite powders with a hierarchically-ordered morphology were synthesized by an ESM template method. The starting materials for this process were $NiCl_2 \cdot 6H_2O$ (Alfa Aesar, 98%), $Ni(NO_3)_2 \cdot 6H_2O$ (Alfa Aesar, 98%), $Ni(CH_3COO)_2 \cdot 4H_2O$ (Alfa Aesar, 98%), $Ce(NO_3)_3 \cdot 6H_2O$ (Aldrich, 99% metal basis), $Gd(NO_3)_3 \cdot xH_2O$ ($x \sim 6$, Alfa Aesar, 99.9%, REO), and ethylene diamine tetra-acetic acid (EDTA) (Alfa Aesar, 99%). The procedure for the synthesis of NiO–GDC powders by the ESM template method is shown in Fig. 1. The synthesis process consists of two steps, including ESM collection and the template process. First, chicken eggshells collected from a local restaurant were cleaned repeatedly to remove the albumen (white part) and remaining yolk. The cleaned eggshells were immersed in an acid tub containing dilute HCl (0.2 M) for 24 h. After digestion of the $CaCO_3$ in the eggshells, the ESMs were collected and washed repeatedly until the membranes were completely free of acid. Finally, the ESMs were dried in an oven overnight at 30 °C. For the template process, a 100 ml stock solution containing $Ni(NO_3)_2 \cdot 6H_2O$, $Ce(NO_3)_3 \cdot 6H_2O$, and $Gd(NO_3)_3 \cdot xH_2O$ was prepared with a stoichiometry amount of cerium and gadolinium of 60 vol% Ni/40 vol% GDC. Since ESM has a tendency to uptake a very small amount of Ni^{2+}, $NiCl_2 \cdot 6H_2O$ and $Ni(CH_3COO)_2 \cdot 4H_2O$ were also used as the precursors. A similar set of three more stock solutions was prepared using EDTA as a chelating agent (EDTA to salt molar ratio = 1). Approximately 6 ml of 0.1 M NaOH was added to completely solubilize EDTA. 10 g of dry ESM was immersed in the prepared stock solution for 24 h and then washed with deionized water to remove the precursor solution on the ESM surface. Subsequently, the hybrid membrane (ESM + precursor ions) was dried for 12 h at 80 °C followed by calcination at 600 °C for 2 h to produce NiO–GDC powder products. The NiO–GDC composites synthesized using Ni chloride, Ni nitrate, and Ni acetate precursor are referred to as NG–C, NG–N, and NG–A, respectively, and those prepared with EDTA are NG–CE, NG–NE, and NG–AE, respectively.

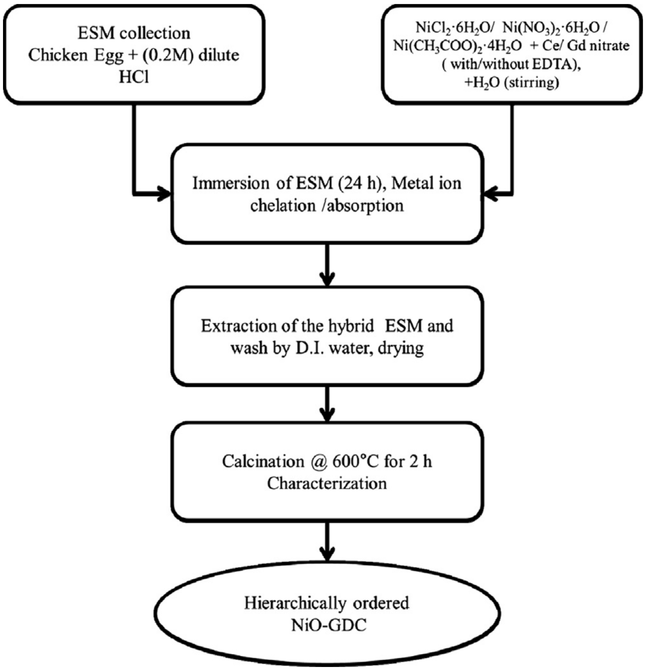

Fig. 1. Flow chart of the synthesis of NiO–GDC powders using ESM templates.

The phases of the as-synthesized NiO–GDC composite powders produced by the ESM template method were characterized by X-ray diffraction (XRD) using Cu (Kα) radiation. The morphology and microstructural characterizations of the powders and sintered bodies were analyzed by scanning electron microscopy/energy-dispersive X-ray spectroscopy (SEM/EDX, SN-3000 Hitachi, Japan). To verify the mechanism of the ESM template process and the pyrolysis process, Fourier transform infrared spectroscopy (FT-IR, Spectrum GX, Perkin Elmer, USA) and thermogravimetric analysis (TGA, TA Q600, TA instruments, USA), respectively, were performed. TGA was performed in air at a temperature range of 30–800 °C at a heating rate of 10 °C min^{-1}.

Electrochemical performance was evaluated by AC impedance spectroscopy and using a single cell test with electrolyte-supported single cells. GDC electrolyte pellets that were 0.5-mm thick and fired at 1450 °C for 4 h were used. $Ba_{0.5}Sr_{0.5}Co_{0.8}Fe_{0.2}O_{3-\delta}$–$Ce_{0.8}Gd_{0.2}O_{1.9}$ (50:50 wt%/wt%) cathode powder synthesized by a combustion method was used as a cathode material [31]. Both anode and cathode pastes prepared by mixing the powder and organic vehicle (Heraeus V006) at a ratio of 70:30 (wt%) were applied to both sides of the GDC electrolyte pellet by a screen printing method, and the electrode area was 0.49 cm^2. Each anode and cathode layer was fired at 1250 °C and 1050 °C for 2 h, respectively. The NiO in the anode was reduced to Ni in humidified H_2 before the electrochemical performance test. AC impedance analysis of the prepared single cell was performed using a universal potentiostat with a frequency response analyzer (Bio-logic science instrument) and a three-electrode configuration under humidified H_2 at 700, 750, and 800 °C. The applied frequency was in the range of 1 mHz to 1 MHz with a voltage amplitude of 10 mV. Current–voltage (*I*–*V*) measurements of the single cells were performed using a fuel cell test station (SMART2, WonATech Co. Ltd, Korea) at 800 °C. Humidified H_2 (~3% H_2O at 30 °C) and dry air were supplied as a fuel and oxidant, respectively, at a rate of 100 cm^3 min^{-1}.

3. Results and discussion

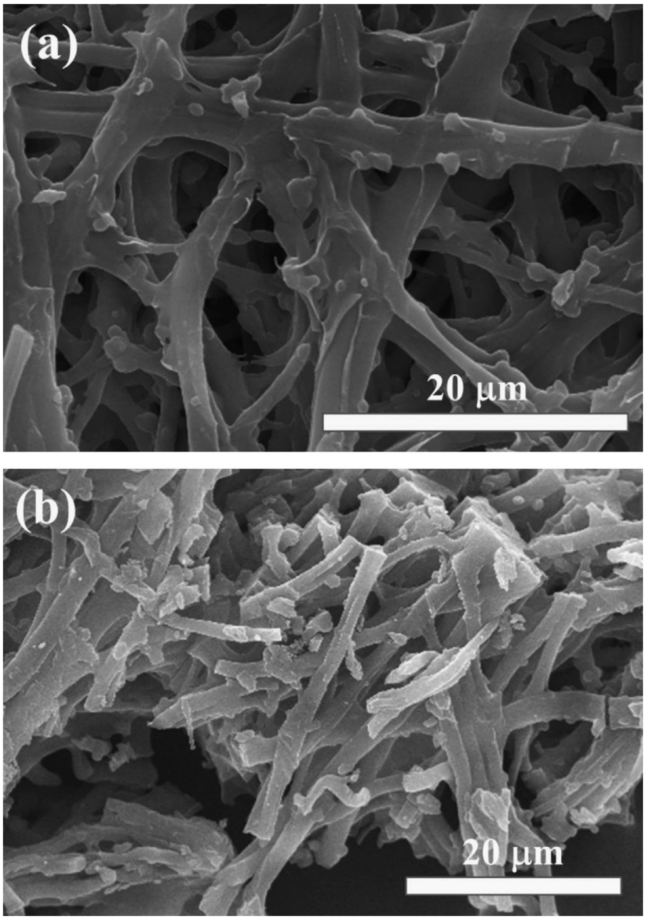

Fig. 2. SEM micrographs of (a) dry ESM collected by acid leaching and (b) hybrid ESM (ESM+NG–AE) after 24 h immersion in the precursor solution.

Fig. 2 shows the microstructures of the dry ESM template and the hybrid membrane after immersion. Raw ESMs have a porous network throughout the laminar structure, and the network structure in the ESM is maintained, even after absorption of metal ions to form a hybrid membrane. The absorption of metal ions through the porous network of the ESM makes it possible to form a hierarchically-ordered structure. ESM exhibits biosorption of various metal ions. The biosorption capacity of the ESM strongly depends upon the type of metal cations, the type of precursor anion, such as sulfate, chloride, nitrate, acetate, and bromide, and the pH of the solutions [21]. Since the surface of the ESM has both negative (–COO$^-$) and positive (–NH^{3+}) charge networks, metal ions, such as Ni^{2+}, Gd^{3+}, and Ce^{3+}, react with –COO$^-$ due to electrostatic interactions through the Coulombic or Van der Waals forces. Therefore, a macroporous-networked morphology can be formed based on the morphology of the ESM, which acts as a scaffold.

ESMs are composed of a glycoprotein matrix, a collagen core, uronic acid, sialic acid, and a number of amino acids. In particular, the collagen and glycoprotein provide the –COO$^-$ and the –NH^{3+} charge networks on the ESM surface [24,25,32]. FT-IR analysis of the hybrid metal ion/ESMs was performed to verify the absorption mechanism of Ni^{2+}, Ce^{3+}, and Gd^{3+} in the porous network of the ESM. Fig. 3 shows typical FT-IR spectra of bare ESM, hybrid ESM, and calcined hybrid ESM. The spectrum of the bare ESM shows a typical peak at 3287 cm^{-1} corresponding to the N–H stretching mode (amide A). Peaks at 3060, 2932, and 2869 cm^{-1} correspond to the =C–H and =CH$_2$ asymmetry stretching modes associated with amide B [33,34]. In the finger point region, peaks at 1630 cm^{-1} (C=O), 1530 cm^{-1} (CN stretching/ NH bending modes), and 1234 cm^{-1} (CN stretching/ NH bending modes) are assigned to the amide I, amide II, and amide III vibrations of the glycoprotein, respectively. These peaks are the characteristic vibration modes of the ESM [35–38]. Other peaks at 1448 cm^{-1} (–C=C stretching mode), 1073 cm^{-1} (C–O stretching mode), and 620 cm^{-1} are also well matched with the FT-IR spectra of the bare ESM reported earlier [35,39,40]. After the bare ESM was immersed in the precursor solution to form the hybrid ESM, the amide I vibration primarily corresponds to the C=O stretching shift from 1630 to 1640 cm^{-1}. This blue shift indicates a change in the hydrogen bond strength of the peptide chains due to the presence of a polar solvent (aqueous solution of Ni/Gd/Ce) and the formation of a new bond between the –COO$^-$ and metal ions [41–43]. However, no significant change in the peak position corresponding to amide II and III in the hybrid ESM was observed. A broad peak at 3330 cm^{-1} corresponding to the –OH vibration mode was also observed, and is superimposed with the N–H stretching signals of the peptides at 3287 cm^{-1}. The peak at 630 cm^{-1} corresponds to a metal hydroxide/oxide stretching mode and/or its superimposed vibration such as δCe–O–C and δNi–O–H vibration [44,45]. Overall, there is significant change in the FT-IR spectra before and after calcination at 600 °C. An intense peak appeared at 495 cm^{-1} after calcination. This peak corresponds to the metal–oxygen stretching mode (<500 cm^{-1}), which indicates the formation of Ni–O, Ce–O, and Gd–O bonds [46–48]. However, the calcined sample also showed distinct peaks at 1210, 1110, and 1050 cm^{-1} corresponding to asymmetric O–C=O, symmetric O–C=O, and C–O stretching, respectively, which are attributed to CO_2 absorbed from the atmosphere. Additionally, the peaks at 3450 and 1630 cm^{-1} corresponding to the –OH stretching may appear due to water adsorbed on the sample surface.

FT-IR spectra of hybrid membranes synthesized from various precursors with and without EDTA are shown in Fig. 4. No significant difference in peak position was observed. Therefore, the adsorption mechanism of metal ions on the ESMs is very similar, regardless of the precursor solutions. While no significant peak shifts were observed for hybrid ESM with and without EDTA, the relative intensity of the major bands increased, which may be due to the polarization of the vibrational mode after metal ion uptake. The effect of EDTA on the hybrid ESM is very difficult to verify from the spectra because both ESM and EDTA have amine groups. In addition, since the NG–CE, NG–NE, and NG–AE hybrid membranes were processed in alkali media (high pH), the conductance of the solvent and the average charge network $–COO^-$ and the $–NH^{3+}$ of ESM could affect the sorption of metal ions [32].

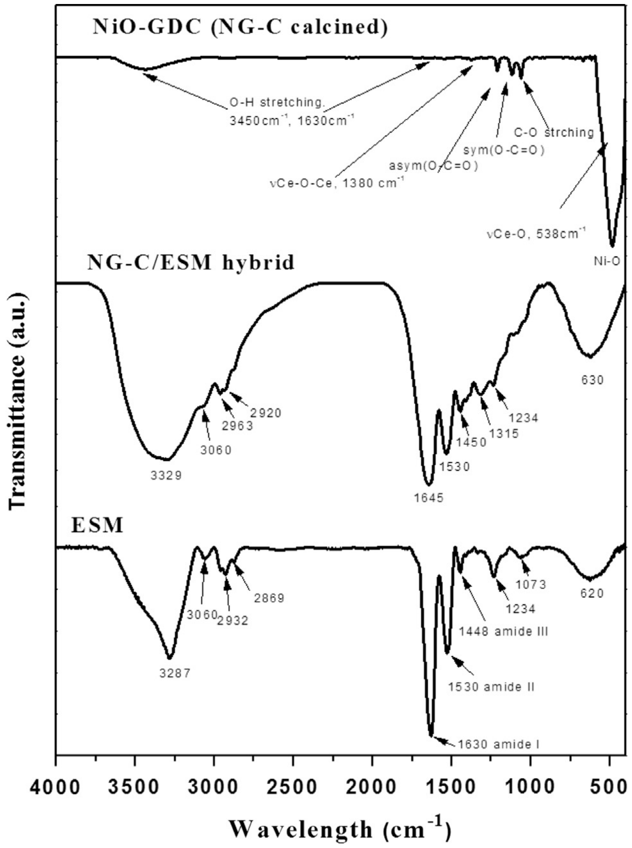

Fig. 3. FT-IR spectra of the bare ESM, the hybrid ESM, and the calcined NiO–GDC (NG–C) powder at 600 °C for 2 h.

The deposited hybrid membranes were analyzed by TGA to understand the thermal behavior of the hybrid ESM and the decomposition process of the metal precursor to form a metal oxide. TGA plots of the hybrid ESMs are shown in Fig. 5. The pyrolysis of the bare ESM typically starts near 250 °C and completes at approximately 600 °C [49,50]. However, the hybrid ESM showed a different trend. The weight loss observed from room temperature to 200 °C is due to the absorbed moisture and water evaporation. The calculated amounts of moisture in the

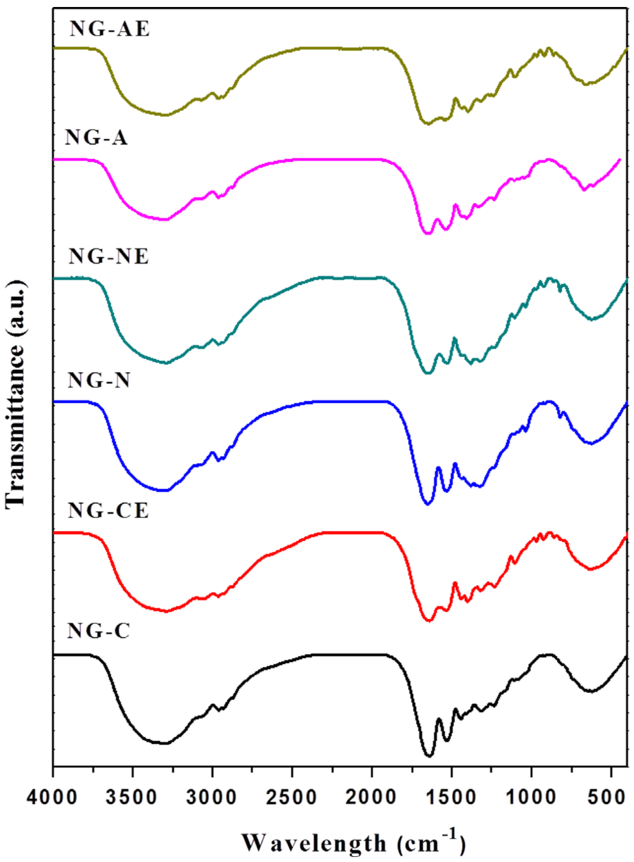

Fig. 4. FT-IR spectra of the hybrid ESMs with various Ni precursors.

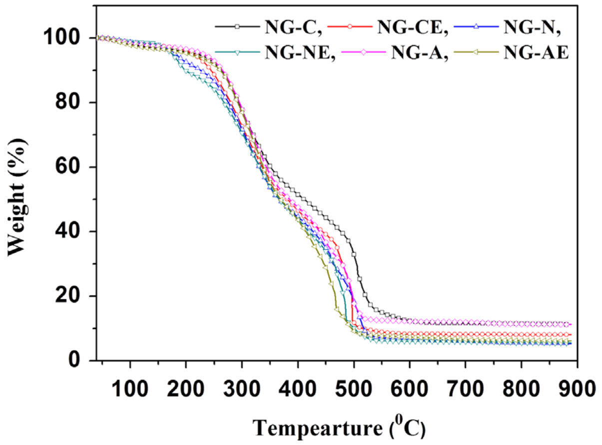

Fig. 5. TGA data of the hybrid ESMs in air.

hybrid ESMs were 3.36, 2.31, 2.02, 2.40, 2.66, and 3.41% the initial weight of the NG–C, NG–CE, NG–N, NG–NE, NG–A, and NG–AE hybrid membranes, respectively. Therefore, the differences in the composition of each hybrid ESM may cause a change in the amount of moisture absorption. With further heating, the weight loss of all the hybrid membranes became saturated at 600 °C. The TGA data shows that the calcination temperature to produce pure NiO–GDC powders should be greater than 600 °C. The pyrolysis of the ESM and the dissociation of the metal precursor to metal oxide may also be completed at 600 °C, and a crystalline NiO–GDC phase is then formed. Furthermore, the decomposition of the metal precursor deposited on the ESM occurred non-linearly, which was observed by the two different slopes in the weight loss curve from 200 to 600 °C. The total weight losses in this temperature range were 85.36% for NG–C, 89.66% for NG–CE, 86.04% for NG–N, 83.38% for NG–NE, 86.07% for NE–A, and 90.43% for NG–AE. The decompositions of the metal precursor for GDC and NiO may occur separately. As all the hybrid membranes have identical nitrate precursors for Ce and Gd, the difference in the slopes of the weight loss for each hybrid ESM may be due to the dissociation of various Ni precursors to form NiO via the Ni-intermediate phases. Various Ni-intermediate phases are formed according to the kind of precursor used. Based on the TGA analysis, the formation of the Ni-intermediate phases occurs at approximately 350 °C. The weight loss for the hybrid ESMs over 200–350 °C was approximately 40 ± 5%. The $Ni(NO_3)_2 \cdot 6H_2O$ precursor forms an intermediate phase of $Ni_3(NO_3)_2(OH)_4$ accompanied by a weight loss of 40% over 250–350 °C [51]. This intermediate $Ni_3(NO_3)_2(OH)_4$ finally transforms to NiO with further heating to 600 °C. Similarly, the intermediate phase for the $Ni(CH_3COO)_2 \cdot 4H_2O$ precursor is $0.86Ni(CH_3COO)_2 \cdot 14Ni(OH)_2$ and the weight loss corresponding to the formation of the intermediate phase is 30.7% [52]. The $NiCl_2 \cdot 6H_2O$ precursor forms an intermediate phase of nickel–hydroxylchloride or nickel–oxychloride accompanied by a weight loss of 49.82% [53]. For the precursor solution with EDTA, the precipitation of $Ni(OH)_2$ is preferable for the formation of Ni-intermediate phases due to the high alkali media (high pH). Thus, the decomposition process starts from $Ni(OH)_2$ without any Ni-intermediate phases, and crystalline NiO is formed.

Fig. 6 shows the yield rate of the final powder product per the unit weight of the hybrid ESM calculated from the TGA data. The amount of metal cations deposited from the precursor solution could be verified by counting the yield rate. Specifically, a high yield rate means that a large amount of metal cations was adsorbed. While the Ni chloride and Ni acetate precursors showed high yield rates of 96.25 and 95.57 mg g^{-1}, respectively, the Ni nitrate precursor had a significantly low rate of 34.37 mg g^{-1}. Therefore, the precursor solution could affect the biosorption of metal cations on the ESM. The presence of chloride ions and acetate ions may enhance the biosorption more than the nitrate ions. Additionally, the presence of a chelating agent such as EDTA resulted in a negative effect on the biosorption capacity of the ESM.

XRD patterns of the as-synthesized NiO–GDC powders calcined at 600 °C for 2 h are shown in Fig. 7. All NiO–GDC powders show a single phase without any trace of secondary or impurity phases, and all peaks are well matched with cubic NiO (Fm3m, JCPDF #47-1049) and cubic $Ce_{0.8}Gd_{0.2}O_{1.9}$ (Fm3m, JCPDF #34-0394). However, the NG–A sample shows very low-intensity NiO peaks. EDS analysis also showed similar results with less Ni (52 vol%) in the NG–A sample detected than the designed amount (60 vol%). Acetate

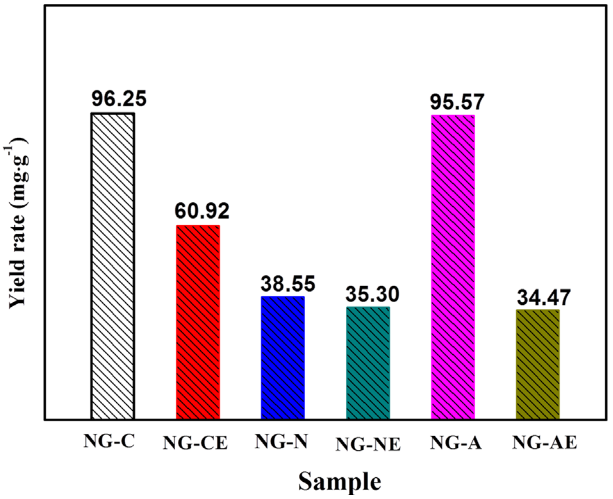

Fig. 6. The calculated yield rates of the as-synthesized NiO–GDC powders according to various precursor solutions.

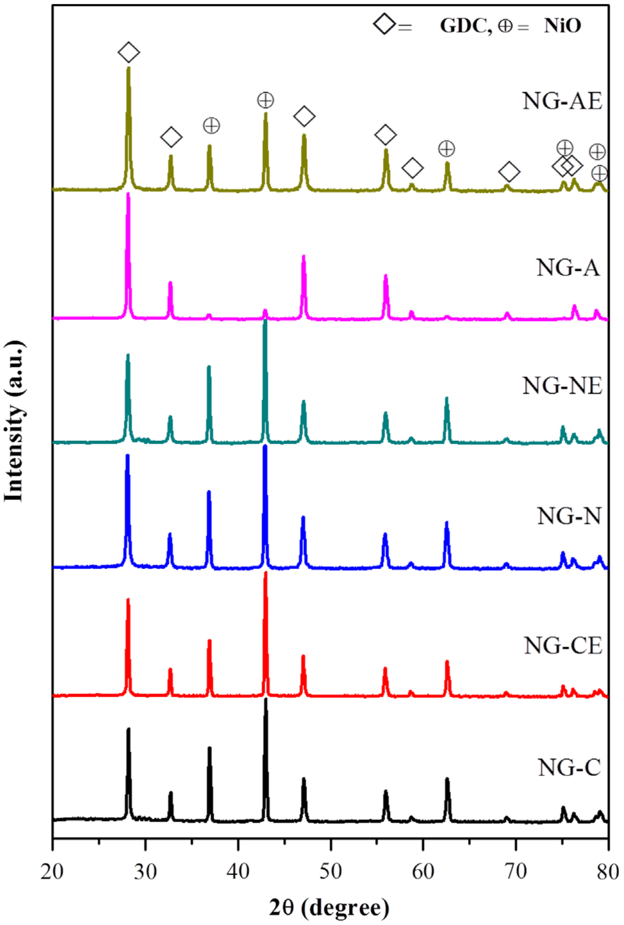

Fig. 7. XRD patterns of the as-synthesized NiO–GDC powders calcined at 600 °C for 2 h.

ions may prevent the ESM from taking Ni^{2+}. Alternatively, when EDTA was used as a chelating agent, this phenomenon was suppressed, as shown in Fig. 7 and the EDS results. Further studies should be performed to verify the effect of EDTA on the Ni^{2+} uptake property of ESMs.

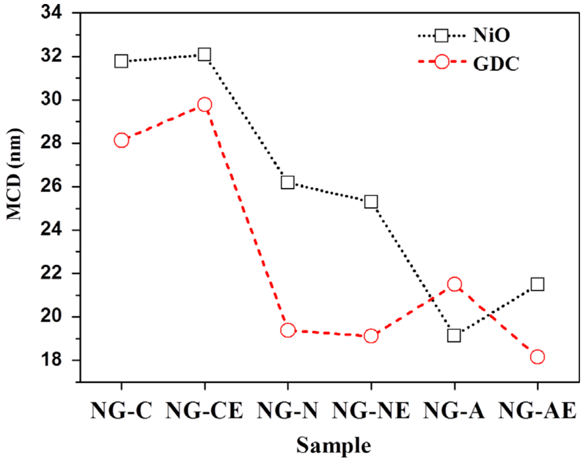

Fig. 8. Variations of mean crystal diameter (MCD) for NiO and GDC in the as-synthesized NiO–GDC composite powders calcined at 600 °C for 2 h.

The variations in the mean crystallite diameters (MCDs) of NiO and GDC in NiO–GDC composite powder, which were calculated using Scherrer's formula, are plotted in Fig. 8. The MCDs of NiO are relatively larger than those of GDC. The initial precursor of Ni also affected the crystalline size. NiO–GDC powders synthesized from Ni chloride precursor had relatively larger crystallite sizes than those synthesized from Ni acetate precursor.

Although there was no significant difference in the crystallite size, the overall morphology of the as-synthesized NiO–GDC powders strongly depended on the initial Ni precursor, as shown in Fig. 9. A hierarchical structure was formed when Ni chloride with EDTA or the Ni acetate precursors were used. While NiO–GDC powders synthesized from Ni acetate precursor held the initial microstructure of the bare ESM with macro-pores, those synthesized from Ni chloride precursor with EDTA had both meso- and micro-pores in the scaffold. Considering the TPB area, anodes with wide pore size distributions would show better electrochemical performance.

Fig. 10 shows SEM micrographs of Ni–GDC anodes on GDC electrolyte sintered at 1250 °C for 2 h. Although it is

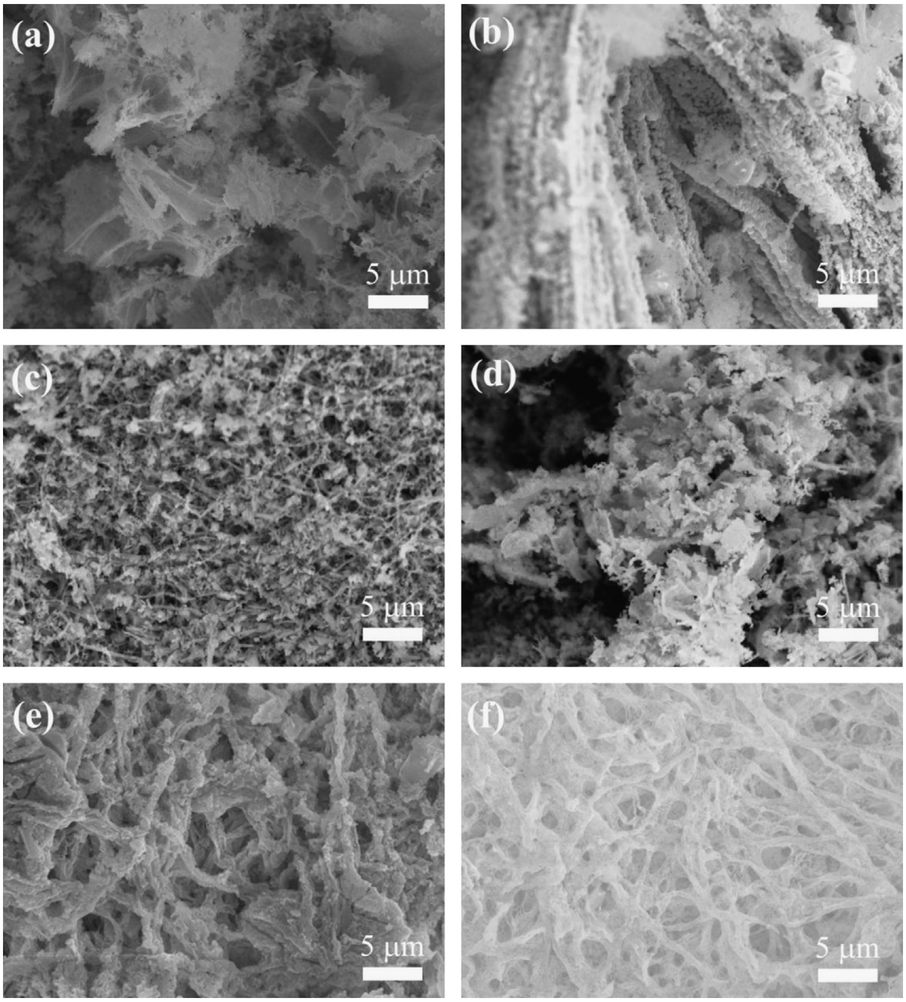

Fig. 9. SEM micrographs of the as-synthesized NiO–GDC powders calcined at 600 °C for 2 h: (a) NG–C, (b) NG–CE, (c) NG–N, (d) NG–NE, (e) NG–A, and (f) NG–AE.

difficult to sustain the initial hierarchical morphology of the as-synthesized powders due to the milling process used to prepare the paste, as well as the high-temperature sintering process, all the anodes still have a small grain size less of than 1 μm, appropriate area contact between the grains, and good adhesion between the anode and electrolyte. In particular, the NG–CE anode has much a smaller grain size and a better-distributed pore structure than the NG–A and NG–AE anodes, which may result in an extension of the TPB area.

The effect of anode morphology on cell performance was investigated by AC impedance spectroscopy. Three different single cells were fabricated using NG–CE, NG–A, and NG–AE anode powders, respectively, because these anodes have hierarchically-ordered morphology. The AC impedance spectra of the Ni–GDC anodes in humidified H_2 at various temperatures are shown in Fig. 11. The high-frequency intercept on the real axis in the impedance spectra can be attributed to the ohmic resistance (R_o), whereas the lower frequency intercept on the real axis indicates the total anode resistance (R_{tot}). The polarization resistance, R_p, is the overall size of the arcs ($R_{tot}-R_o$). The R_p values calculated at 700, 750, and 800 °C are shown in Table 1. The NG–CE anode showed the lowest R_p value at a given temperature in H_2. The temperature dependences of the ohmic (R_o) and polarization

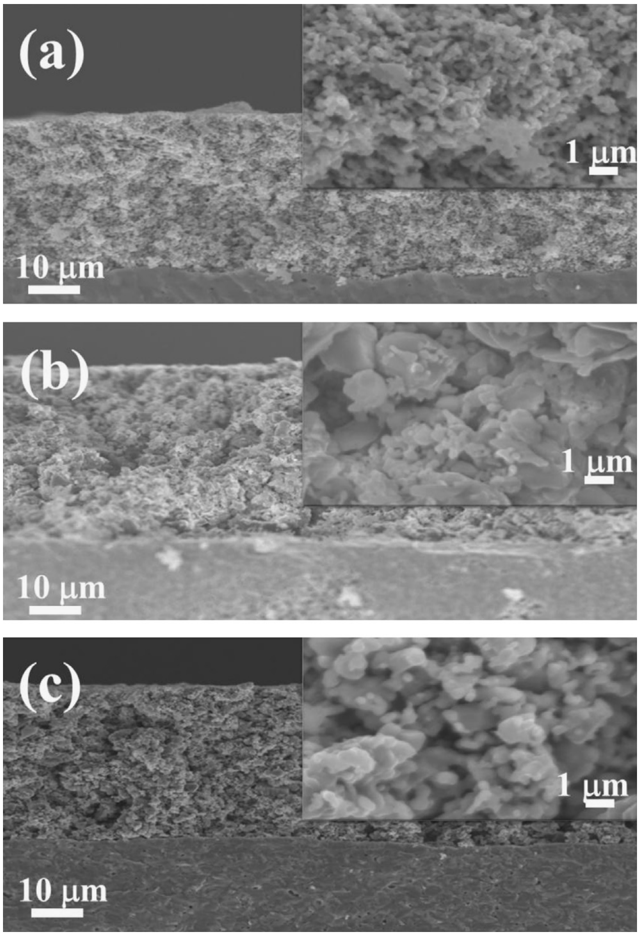

Fig. 10. SEM micrographs of the NiO–GDC anodes of (a) NG–CE, (b) NG–A, and (c) NG–AE fired at 1250 °C for 2 h. The inset shows an enlarged micrograph of the anode region.

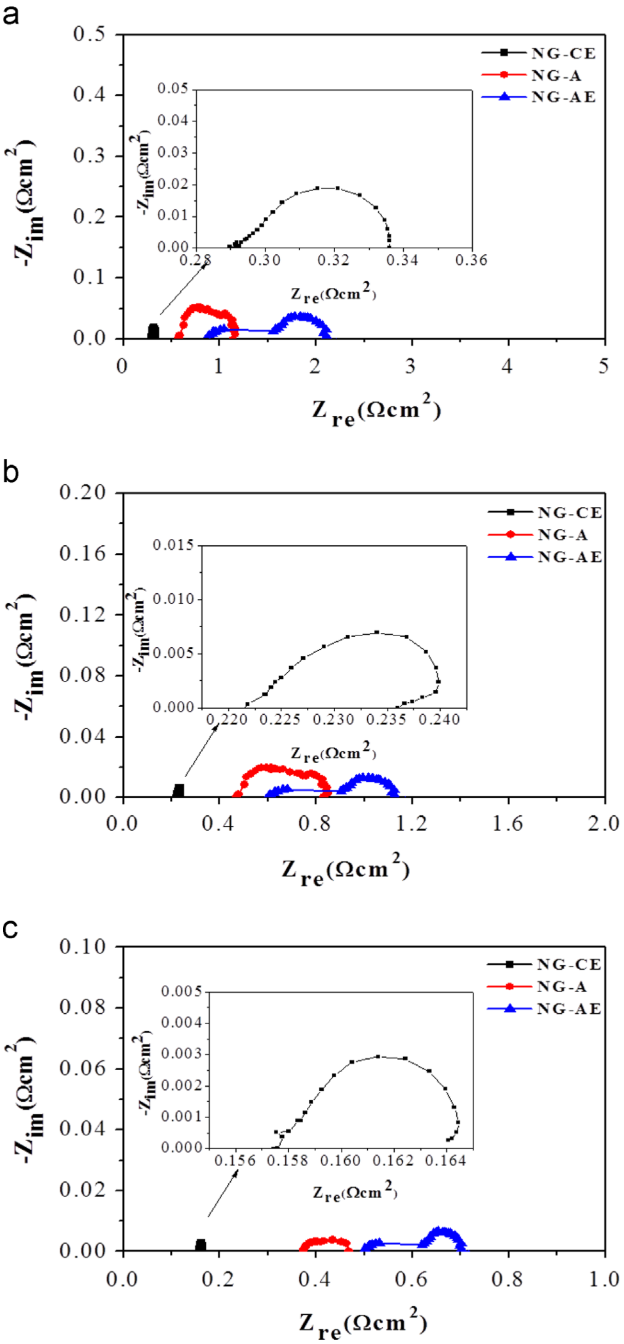

Fig. 11. Typical AC impedance spectra of Ni–GDC anodes at (a) 700 °C, (b) 750 °C, and (c) 800 °C in humidified H_2.

Table 1
Polarization resistance and activation energy of the Ni–GDC anodes at various operating temperatures in humidified H_2.

Anode material	Polarization resistance (Ω cm^2)			Activation energy (eV)
	700 °C	750 °C	800 °C	
NG–CE	0.044	0.015	0.007	0.74
NG–A	0.568	0.364	0.094	0.75
NG–AE	1.206	0.533	0.205	0.77

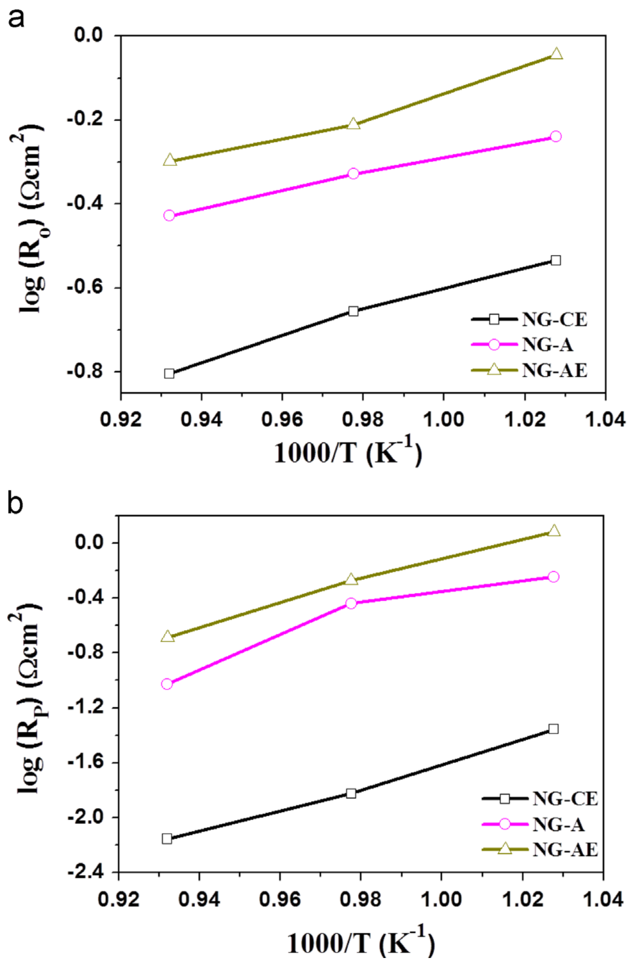

Fig. 12. Temperature dependence of (a) ohmic (R_o) and (b) polarization (R_p) resistances of Ni–GDC anodes in humidified H_2.

(R_p) resistances are shown in Fig. 12, and the calculated activation energy values, E_a, are shown in Table 1. The NG–CE anodes exhibited lower R_o and R_p values than the NG–A and the NG–AE anodes. Since the electrochemical performance was strongly affected by the electrode microstructure, which restrains the reaction sites, the NG–CE anode with the smaller grain size and the better-distributed pore structure, as shown in Fig. 10, exhibits the best performance. The relatively poor electrochemical performance of the NG–AE anode could be partly due to the use of less Ni catalyst (52 vol%) than the other anodes (~60 vol%) and the microstructure. Moreover, the activation energies of these anodes fabricated with hierarchically-ordered NiO–GDC powders are less than previously reported. The activation energy of pure Ni, a Ni-impregnated GDC composite anode, and a GDC-impregnated Ni composite anode were previously demonstrated to be 0.871, 0.757, and 0.829 eV, respectively [54–56].

The cell voltages and power densities with current density for the Ni–GDC anodes (NG–CE, NG–A, and NG–AE) are shown in Fig. 13. The open circuit voltages at 800 °C were 0.7 ± 0.02 V due to the reduction of the GDC electrolyte in the reducing atmosphere. The maximum power density of the single cell with the NG–CE anode was 0.34 W cm^{-2}, which was greater than those of the single cells with the NG–A (0.32 W cm^{-2}) and NG–AE (0.28 W cm^{-2}) anodes. This result is consistent with the trend observed in the AC impedance data. The difference in electrochemical performance could be attributed to the microstructure of the anodes, as shown in Fig. 10. Although the Ni–GDC anodes synthesized by the ESM template method showed enhanced single cell performance compared with other conventional anode materials, considering the 500-μm thick electrolyte, the overall electrochemical performance of the single cell could be further improved. Therefore, optimization of the ESM template process to control the chemical composition is required. Additional studies using novel fabrication processes, such as the casting method, would make it possible to maintain an initial hierarchically-ordered structure throughout the electrode fabrication steps, including the sintering process, in order to enhance the overall cell performance.

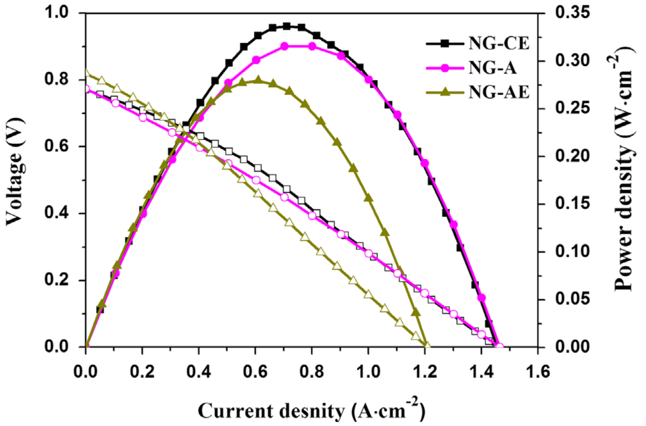

Fig. 13. Comparison of the *I–V* curves (open symbols) and power densities (closed symbols) of Ni–GDC anodes at 800 °C with a humidified H_2 fuel.

4. Conclusions

A novel biogenic template method was developed using ESMs to synthesize hierarchically-ordered NiO–GDC anode materials for SOFC. Glycoproteins in the ESM are responsible for the biosorption of the metal ions to form hierarchically-ordered morphology. The type of Ni precursor, such as chloride, nitrate, or acetate, and the use of EDTA as a chelating agent could affect the uptake property of the ESM for metal ions and morphology. Both Ni chloride and acetate precursors with EDTA were suitable for the synthesis of anode materials with hierarchically-ordered morphology. The hierarchically-ordered NiO–GDC anodes prepared by the ESM template method exhibited much lower polarization resistance and activation energy than conventional Ni-based anode materials. Therefore, the ESM template method is very appropriate for fabricating highly-efficient anode materials for SOFCs. Nevertheless, it is essential to optimize the concentration of the precursor solution to ensure high productivity and to develop advanced processes to sustain the initial morphology through to the final sintering step of cell fabrication. However, this technique could be very attractive for other energy materials, such as batteries, catalysts, and chemical sensors, which do not require high-temperature treatments to form a desired microstructure.

Acknowledgments

This research was supported by a grant from the Fundamental R&D Program for Core Technology of Materials funded by the Ministry of Knowledge Economy, Republic of Korea. This work was also supported by the Human Resources Development of the Korea Institute of Energy Technology Evaluation and Planning (KETEP) grant funded by the Korea Government Ministry of Knowledge Economy (No. 20114030200060).

References

[1] N.Q. Minh, Ceramic fuel cells, Journal of the American Ceramic Society 76 (1993) 563–588.

[2] S.C. Singhal, Advances in solid oxide fuel cell technology, Solid State Ionics 135 (2000) 305–313.

[3] T. Suzuki, Z. Hasan, Y. Funahashi, T. Yamaguchi, Y. Fujishiro, M. Awano, Impact of anode microstructure on solid oxide fuel cells, Science 325 (2009) 852–855.

[4] C. Xia, M. Liu, Novel cathodes for low-temperature solid oxide fuel cells, Advanced Materials 14 (2002) 521–523.

[5] P.W. Li, M.K. Chyu, Electrochemical and transport phenomena in solid oxide fuel cells, Journal of Heat Transfer 127 (2005) 1344–1362.

[6] J.W. Kim, A.V. Virkar, K.Z. Fung, K. Mehta, S.C. Singhal, Polarization effects in intermediate temperature, anode-supported solid oxide fuel cells, Journal of the Electrochemical Society 146 (1999) 69–78.

[7] P. Costamagna, P. Costa, V. Antonucci, Micro-modelling of solid oxide fuel cell electrodes, Electrochimica Acta 43 (1998) 375–394.

[8] Y. Suzue, N. Shikazono, N. Kasagi, Micro modeling of solid oxide fuel cell anode based on stochastic reconstruction, Journal of Power Sources 184 (2008) 52–59.

[9] T. Fukui, K. Murata, S. Ohara, H. Abe, M. Naito, K. Nogi, Morphology control of Ni–YSZ cermet anode for lower temperature operation of SOFCs, Journal of Power Sources 125 (2004) 17–21.

[10] S.P. Yoon, S.W. Nam, J. Han, T.H. Lim, S.A. Hong, S.H. Hyun, Effect of electrode microstructure on gas-phase diffusion in solid oxide fuel cells, Solid State Ionics 166 (2004) 1–11.

[11] S.W. Jung, J.M. Vohs, R.J. Gorte, Preparation of SOFC anodes by electrodeposition, Journal of the Electrochemical Society 154 (2007) B1270–B1275.

[12] D. Dong, Z. Chai, C.Z. Li, H. Wang, Polymer hydrogel assisted combustion synthesis of highly crystalline ceramic nanoparticles for SOFC electrolyte films, Materials Chemistry and Physics 118 (2009) 148–152.

[13] X.L. Weng, D. Brett, V. Yufit, P. Shearing, N. Brandon, M. Reece, H. X. Yan, C. Tighe, J.A. Darr, Highly conductive low nickel content nanocomposite dense cermets from nano-powders made via a continuous hydrothermal synthesis route, Solid State Ionics 181 (2010) 827–834.

[14] T. Razpotnik, M. Marinsek, B. Novosel, K. Zupan, V. Francetic, J. Macek, A polymer complex solution process for the synthesis and characterization of Ni–YSZ cermet material, Ceramics International 34 (2008) 1741–1746.

[15] S.D. Kim, J.J. Lee, H. Moon, S.H. Hyun, J. Moon, J. Kim, H.W. Lee, Effects of anode and electrolyte microstructures on performance of solid oxide fuel cells, Journal of Power Sources 169 (2007) 265–270.

[16] G.Q. Shao, H. Cai, J.R. Xie, X.L. Duan, B.L. Wu, R.Z. Yuan, J.K. Guo, Preparation of nanocomposite Ni/YSZ cermet powder by EDTA complexes–gel conversion process, Materials Letters 57 (2003) 3287–3290.

[17] H. Shimada, E. Takami, K. Takizawa, A. Hagiwara, M. Ihara, Highly dispersed anodes for solid oxide fuel cells using NiO/YSZ/BZY triple-phase composite powders prepared by spray pyrolysis, Solid State Ionics 193 (2011) 43–51.

[18] W.C. Jung, J.O. Dereux, W.C. Chueh, Y. Hao, S.M. Haile, High electrode activity of nanostructured, columnar ceria films for solid oxide fuel cells, Energy and Environmental Science 5 (2012) 8682–8689.

[19] Y. Wu, W. Wang, K. Wang, Y. Zeng, D. Dong, Z. Shao, H. Wang, Morphology and catalytic performance of flake-shaped NiO–yttria-stabilized zirconia (YSZ) particles with nanocrystalline YSZ grains, Industrial and Engineering Chemistry Research 51 (2012) 6387–6394.

[20] H. Zhou, T. Fan, D. Zhang, Biotemplated materials for sustainable energy and environment: current status and challenges, Chemistry and Sustainability, Energy and Materials 4 (2011) 1344–1387.

[21] K. Suyama, Y. Fukazawa, Y. Umetsu, A new biomaterial, hen egg shell membrane, to eliminate heavy metal ion from their dilute waste solution, Applied Biochemistry and Biotechnology 45–46 (1994) 871–879.

[22] D. Yang, L. Qi, J. Ma, Eggshell membrane templating of hierarchically ordered macroporous networks composed of TiO_2 tubes, Advanced Materials 14 (2002) 1543–1546.

[23] P.K. Ajikumar, R. Lakshminarayanan, S. Valiyaveettil, Controlled deposition of thin films of calcium carbonate on natural and synthetic templates, Crystal Growth and Design 4 (2004) 331–336.

[24] C. Shao, B. Yuan, H. Wang, Q. Zhou, Y. Li, Y. Guan, Z. Deng, Eggshell membrane as a multimodal solid state platform for generating fluorescent metal nanoclusters, Journal of Materials Chemistry 21 (2011) 2863–2866.

[25] H. Su, Q. Dong, J. Han, D. Zhang, Q. Guo, Biogenic synthesis and photocatalysis of Pd–PdO nanoclusters reinforced hierarchical TiO_2 films with interwoven and tubular conformations, Biomacromolecules 9 (2008) 499–504.

[26] Q. Tang, Z. Tang, J. Wu, J. Lin, M. Huang, A facile route to a macroporous silver network for methanol oxidation, RSC Advances 1 (2011) 1453–1456.

[27] J. Liu, Y. Zhou, J. Wang, Y. Pan, D. Xue, Template-free solvothermal synthesis of yolk–shell V_2O_5 microspheres as cathode materials for Li-ion batteries, Chemical Communications 47 (2011) 10380–10382.

[28] D. Yang, L. Qi, J. Ma, Hierarchically ordered networks comprising crystalline ZrO_2 tubes through sol–gel mineralization of eggshell membranes, Journal of Materials Chemistry 13 (2003) 1119–1123.

[29] J. Li, K.L. Chiu, F.L. Kwong, D.H.L. Ng, S.L.I. Chan, Conversion of egg shell membrane to inorganic porous $Ce_xZr_{1-x}O_2$ fibrous network, Current Applied Physics 9 (2009) 1438–1444.

[30] D. Dong, Y. Wu, X. Zhang, J. Yao, Y. Huang, D. Li, C.Z. Li, H. Wang, Eggshell membrane-templated synthesis of highly crystalline perovskite ceramics for solid oxide fuel cells, Journal of Materials Chemistry 21 (2011) 1028–1032.

[31] M.K. Rath, B.H. Choi, K.T. Lee, Properties and electrochemical performance of $La_{0.75}Sr_{0.25}Cr_{0.5}Mn_{0.5}O_{3-\delta}$–$La_{0.2}Ce_{0.8}O_{2-\delta}$ composite anodes for solid oxide fuel cells, Journal of Power Sources 213 (2012) 55–62.

[32] B. Liu, Y. Huang, Polyethyleneimine modified eggshell membrane as a novel biosorbent for adsorption and detoxification of Cr(VI) from water, Journal of Materials Chemistry 21 (2011) 17413–17418.

[33] T. Weymuth, C.R. Jacob, M. Reiher, A local-mode model for understanding the dependence of the extended amide III vibrations on protein secondary structure, The Journal of Physical Chemistry B 114 (2010) 10649–10660.

[34] K. Kaiden, T. Matsui, S. Tanaka, A study of the amide III band by FT-IR spectrometry of the secondary structure of albumin, myoglobin, and γ-globulin, Applied Spectroscopy 41 (1987) 180–184.

[35] Q. Dong, H. Su, D. Zhang, W. Cao, N. Wang, Biogenic synthesis of tubular SnO_2 with hierarchical intertextures by an aqueous technique involving glycoprotein, Langmuir 23 (2007) 8108–8113.

[36] J. Banker, Amide modes and protein conformation, Biochimica et Biophysica Acta 1120 (1992) 123–143.

[37] M. Arami, N.Y. Limaee, N.M. Mahmoodi, Investigation on the adsorption capability of egg shell membrane towards model textile dyes, Chemosphere 65 (2006) 1999–2008.

[38] J. Kong, S. Yu, Fourier transform infrared spectroscopic analysis of protein secondary structures, Acta Biochimica et Biophysica Sinica 39 (2007) 549–559.

[39] Y.H. Zhao, Y.U. Chi, Characterization of collagen from eggshell membrane, Biotechnology 8 (2009) 254–258.

[40] W.T. Tsai, J.M. Yang, C.W. Lai, Y.H. Cheng, C.C. Lin, C.W. Yeh, Characterization and adsorption properties of eggshells and eggshell membrane, Bioresource Technology 97 (2006) 488–493.

[41] J. Kubelka, T.A. Keiderling, Ab initio calculation of amide carbonyl stretch vibrational frequencies in solution with modified basis sets. 1. N-methyl acetamide, The Journal of Physical Chemistry A 105 (2001) 10922–10928.

[42] R. Wieczorek, J.J. Dannenberg, Amide I vibrational frequencies of α-helical peptides based upon ONIOM and density functional theory (DFT) studies, The Journal of Physical Chemistry B 112 (2008) 1320–1328.

[43] K.M. Gough, D. Zelinski, R. Wiens, M. Rak, I.M.C. Dixon, Fourier transform infrared evaluation of microscopic scarring in the cardiomyopathic heart: effect of chronic AT1 suppression, Analytical Biochemistry 316 (2003) 232–242.

[44] T.N. Ramesh, P.V. Kamath, Synthesis of nickel hydroxide: effect of precipitation conditions on phase selectivity and structural disorder, Journal of Power Sources 156 (2006) 655–661.

[45] P.V. Kamath, G.N. Subbanna, Electroless nickel hydroxide: synthesis and characterization, Journal of Applied Electrochemistry 22 (1992) 478–482.

[46] F. Porta, S. Recchia, C. Bianchi, F. Confalonieri, G. Scari, Synthesis and full characterisation of nickel(II) colloidal particles and their transformation into NiO, Colloids and Surfaces A 155 (1999) 395–404.

[47] N. Parvatikar, S. Jain, S.V. Bhoraskar, M.V.N.A. Prasad, Spectroscopic and electrical properties of polyaniline/CeO_2 composites and their application as humidity sensor, Journal of Applied Polymer Science 102 (2006) 5533–5537.

[48] B. Yan, H. Zhu, Controlled synthesis of CeO_2 nanoparticles using novel amphiphilic cerium complex precursors, Journal of Nanoparticle Research 10 (2008) 1279–1285.

[49] Q. Wang, Z. Jiang, Y. Wang, D. Chen, D. Yang, Photocatalytic properties of porous C-doped TiO_2 and Ag/C-doped TiO_2 nanomaterials by eggshell membrane templating, Journal of Nanoparticle Research 11 (2009) 375–384.

[50] F. Yi, Z.X. Guo, L.X. Zhang, J. Yu, Q. Li, Soluble eggshell membrane protein: preparation, characterization and biocompatibility, Biomaterials 25 (2004) 4591–4599.

[51] J. Estelle, P. Salagre, Y. Cesteros, M. Serra, F. Medina, J.E. Sueiras, Comparative study of the morphology and surface properties of nickel oxide prepared from different precursors, Solid State Ionics 156 (2003) 233–243.

[52] J.C. De Jesus, I. Gonzalez, A. Quevedo, T. Puerta, Thermal decomposition of nickel acetate tetrahydrate: an integrated study by TGA, QMS and XPS techniques, Journal of Molecular Catalysis A: Chemical 228 (2005) 283–291.

[53] S.K. Mishra, S.B. Kanungo, Thermal dehydration and decomposition of nickel chloride hydrate ($NiCl_2 \cdot xH_2O$), Journal of Thermal Analysis and Calorimetry 38 (1992) 2417–2436.

[54] A. Bieberle, L.P. Meier, L.J. Gauckler, The electrochemistry of Ni pattern anodes used as solid oxide fuel cell model electrodes, Journal of the Electrochemical Society 148 (2001) A646–A656.

[55] S.P. Jiang, S. Zhang, Y.D. Zhen, A.P. Koh, Performance of GDC-impregnated Ni anodes of SOFCs, Electrochemical and Solid-State Letters 7 (2004) A282–A285.

[56] U.P. Muecke, K. Akiba, A. Infortuna, T. Salkus, N.V. Stus, L.J. Gauckler, Electrochemical performance of nanocrystalline nickel/gadolinia-doped ceria thin film anodes for solid oxide fuel cells, Solid State Ionics 178 (2008) 1762–1768.